



Aberystwyth University

Constraining variable density of ice shelves using wide-angle radar measurements

Drews, Reinhard; Brown, Joel; Matsuoka, Kenichi; Witrant, Emmanuel; Philippe, Morgane; Hubbard, Bryn; Pattyn, Frank

Published in:
Cryosphere

DOI:
[10.5194/tc-10-811-2016](https://doi.org/10.5194/tc-10-811-2016)

Publication date:
2016

Citation for published version (APA):

Drews, R., Brown, J., Matsuoka, K., Witrant, E., Philippe, M., Hubbard, B., & Pattyn, F. (2016). Constraining variable density of ice shelves using wide-angle radar measurements. *Cryosphere*, 10(2), 811-823. <https://doi.org/10.5194/tc-10-811-2016>

Document License CC BY

General rights

Copyright and moral rights for the publications made accessible in the Aberystwyth Research Portal (the Institutional Repository) are retained by the authors and/or other copyright owners and it is a condition of accessing publications that users recognise and abide by the legal requirements associated with these rights.

- Users may download and print one copy of any publication from the Aberystwyth Research Portal for the purpose of private study or research.
- You may not further distribute the material or use it for any profit-making activity or commercial gain
- You may freely distribute the URL identifying the publication in the Aberystwyth Research Portal

Take down policy

If you believe that this document breaches copyright please contact us providing details, and we will remove access to the work immediately and investigate your claim.

tel: +44 1970 62 2400
email: is@aber.ac.uk



Constraining variable density of ice shelves using wide-angle radar measurements

Reinhard Drews¹, Joel Brown², Kenichi Matsuoka³, Emmanuel Witrant⁴, Morgane Philippe¹, Bryn Hubbard⁵, and Frank Pattyn¹

¹Laboratoire de Glaciologie, Université Libre de Bruxelles, Brussels, Belgium

²Aesir Consulting LLC, Missoula, MT, USA

³Norwegian Polar Institute, Tromsø, Norway

⁴Université Grenoble Alpes/CNRS, Grenoble Image Parole Signal Automatique, 38041 Grenoble, France

⁵Aberystwyth University, Aberystwyth, Wales, UK

Correspondence to: Reinhard Drews (rdrews@ulb.ac.be)

Received: 23 September 2015 – Published in The Cryosphere Discuss.: 21 October 2015

Revised: 19 March 2016 – Accepted: 31 March 2016 – Published: 15 April 2016

Abstract. The thickness of ice shelves, a basic parameter for mass balance estimates, is typically inferred using hydrostatic equilibrium, for which knowledge of the depth-averaged density is essential. The densification from snow to ice depends on a number of local factors (e.g., temperature and surface mass balance) causing spatial and temporal variations in density–depth profiles. However, direct measurements of firn density are sparse, requiring substantial logistical effort. Here, we infer density from radio-wave propagation speed using ground-based wide-angle radar data sets (10 MHz) collected at five sites on Roi Baudouin Ice Shelf (RBIS), Dronning Maud Land, Antarctica. We reconstruct depth to internal reflectors, local ice thickness, and firn-air content using a novel algorithm that includes traveltime inversion and ray tracing with a prescribed shape of the depth–density relationship. For the particular case of an ice-shelf channel, where ice thickness and surface slope change substantially over a few kilometers, the radar data suggest that firn inside the channel is about 5 % denser than outside the channel. Although this density difference is at the detection limit of the radar, it is consistent with a similar density anomaly reconstructed from optical televiewing, which reveals that the firn inside the channel is 4.7 % denser than that outside the channel. Hydrostatic ice thickness calculations used for determining basal melt rates should account for the denser firn in ice-shelf channels. The radar method presented here is robust and can easily be adapted to different radar frequencies and data-acquisition geometries.

1 Introduction

As a snow layer deposited at the ice-sheet surface is progressively buried by subsequent snowfall, it transforms to higher-density firn under the overburden pressure. The firn–ice transition, marked by the depth at which air bubbles are isolated, occurs at a density of approximately 830 kg m^{-3} at depths typically ranging from 30 to 120 m in polar regions (Cuffey and Paterson, 2010, Chapter 2). Densification continues until air bubbles transform to clathrate hydrates and pure ice density is reached ($\rho_i \approx 917 \text{ kg m}^{-3}$). The precise nature of this densification depends on a number of local factors that also vary temporally (Arthern et al., 2010), including surface density and stratification (Hörhold et al., 2011), surface mass balance and temperature (e.g., Herron and Langway, 1980), as well as dynamic recrystallization and the strain regime. Recent studies also highlight the role of microstructure (Gregory et al., 2014) and impurities (Hörhold et al., 2012; Freitag et al., 2013a, b).

Knowledge of the depth–density profile and its spatial and temporal variability is important for a number of applications: (i) to determine the age difference of enclosed air bubbles and the surrounding ice in ice cores (Bender et al., 1997); (ii) to determine the depth and the cumulative mass above radar reflectors in order to map surface mass balance with radar (Waddington et al., 2007; Eisen et al., 2008); (iii) to interpret the seasonality of surface elevation changes (Zwally and Jun, 2002; Ligtenberg et al., 2014) in terms of surface mass balance, firn compaction, and dynamic thin-

ning (e.g., Wouters et al., 2015); and (iv) to infer ice-shelf thickness for mass balance estimates (Rignot et al., 2013; Depoorter et al., 2013) from hydrostatic equilibrium (Griggs and Bamber, 2011).

Density profiles are most reliably retrieved from ice/firn cores either by measuring discrete samples gravimetrically, or by using continuous dielectric profiling (Wilhelms et al., 1998) or X-ray tomography (Kawamura, 1990; Freitag et al., 2013a). Techniques such as gamma-, neutron-, laser-, or optical-scattering (Hubbard et al., 2013, and references therein) circumnavigate the labor-intensive retrieval of an ice core and only require a borehole, which can rapidly be drilled using hot water.

All of the aforementioned techniques, however, remain point measurements requiring substantial logistics. A complementary approach is to exploit the density dependence of radio-wave propagation speed. The principle underlying the technique involves illuminating a reflector with different ray paths such that both the reflector depth and the radio-wave propagation speed may be calculated using methods such as the Dix inversion (Dix, 1955), semblance analysis (e.g., Booth et al., 2010, 2011), interferometry (Arthern et al., 2013), or traveltimes inversion based on ray tracing (Zelt and Smith, 1992; Brown et al., 2012).

A typical acquisition geometry is to position receiver and transmitter with variable offsets so that the subsurface reflection point remains the same for horizontal reflectors (common-midpoint surveys, e.g. Murray et al., 2000; Winebrenner et al., 2003; Hempel et al., 2000; Eisen et al., 2002; Bradford et al., 2009; Blindow et al., 2010). Alternatively, only the receiver can be moved (Fig. 1) resulting in what is sometimes referred to as wide-angle reflection and refraction (WARR; Hubbard and Glasser, 2005, p. 165) geometry. In all cases, density can be inferred from the radar-wave speed using density–permittivity relations (e.g., Looyenga, 1965; Wharton et al., 1980; Kovacs et al., 1995).

Here, we investigate six WARR measurements collected in December 2013 on Roi Baudouin Ice Shelf (RBIS), Dronning Maud Land, Antarctica. The WARR sites are part of a larger geophysical survey imaging an ice-shelf pinning-point and a number of ice-shelf channels which are about 2 km wide and can extend longitudinally from the grounding line to the ice-shelf front (Le Brocq et al., 2013). Ice inside the channels is thinner, sometimes more than 50% (Drews, 2015), and the surface is depressed, causing the elongated lineations visible in satellite imagery (Fig. 2). Basal melting inside channels can be significantly larger (Stanton et al., 2013), correspondingly influencing ice-shelf stability (Sergienko, 2013). Adjustment towards hydrostatic equilibrium resulting from basal melting can weaken ice shelves through crevasse formation (Vaughan et al., 2012). Channelized melting, on the other hand, can also prevent excessive area-wide basal melting and hence stabilize ice shelves (Gladish et al., 2012; Millgate et al., 2013).

The basal mass balance inside ice-shelf channels can be mapped from remote sensing assuming mass conservation (e.g., Dutrieux et al., 2013). This approach calculates ice thickness from hydrostatic equilibrium which engenders potentially two pitfalls. (i) Bridging stresses can prevent full relaxation to hydrostatic equilibrium (Drews, 2015), and (ii) it may not account for small-scale variations in material density. Evidence for small-scale changes in density was suggested by Langley et al. (2014) and Drews (2015), who found that the surface mass balance can be elevated locally within the concave surface associated with ice-shelf channels, which in turn may impact the local densification processes. Atmospheric models typically operate with a horizontal gridding coarser than 5 km (Lenaerts et al., 2014) and cannot resolve such small-scale variations in surface mass balance and density.

Herein, we calculate densities from WARR sites using traveltimes inversion and ray tracing (Sect. 2). The data set is supplemented with densities based on optical televueing (OPTV) of two boreholes (Fig. 2; Sect. 3). In Sects. 4 and 5, we compare both methods and discuss density anomalies associated with the ice-shelf channels. We present our conclusions about the derivation of density from radar in general, and the density anomalies in ice-shelf channels in particular in Sect. 6, and discuss consequences of our findings for estimating basal melt rates in ice-shelf channels.

2 Development of a new algorithm to infer density from wide-angle radar

We describe the propagation of the radar wave for each offset as a ray traveling from the transmitter via the reflection boundary to the receiver (Fig. 1). Using a coordinate system, where x is parallel to the surface and z points vertically downwards, the ray paths are determined by the spatially variable radio-wave propagation speed $v(x, z)$ which is primarily determined by density; unless $v(x, z)$ is constant, ray paths are not straight but bend following Fermat's principle of minimizing the traveltimes between transmitter and receiver. The geometry depicted in Fig. 1 is common in seismic investigations, and multiple techniques exist for deriving the velocities from recorded traveltimes (Yilmaz, 1987).

Similar to what has been done for wide-angle radar measurements in Greenland (Brown et al., 2012), we follow a variation of the approach delineated by Zelt and Smith (1992). Brown et al. (2012) measured common midpoint returns with a 100 MHz radar. They used a ray tracing forward model and inferred bulk densities of individual intervals (hereafter interval densities) by inverting reflector depths and interval velocities for single reflectors from top to bottom (a.k.a. layer stripping). In this paper, we use a 10 MHz radar providing improved depth penetration at the expense of lower spatial resolution. In order to prevent small errors in interval densities and velocities associated with shallow reflec-

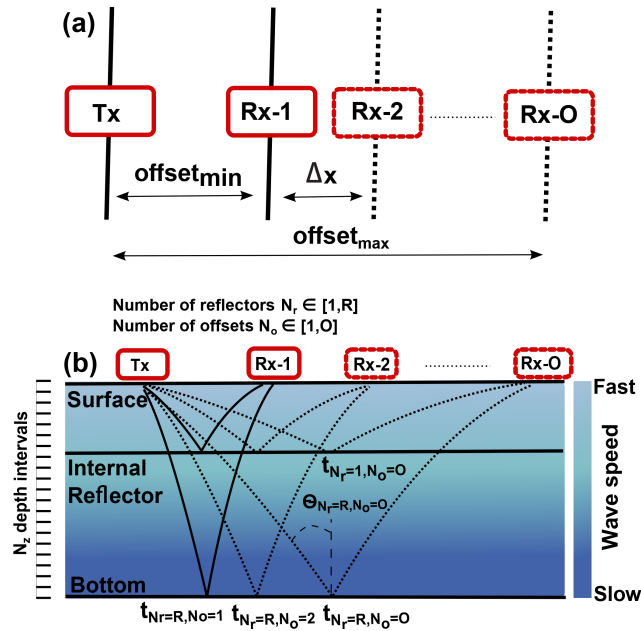


Figure 1. (a) Plain view of the wide-angle acquisition geometry: transmitting (Tx) and receiving (Rx) antennas were aligned in parallel. While the transmitter remained at a fixed location, the receiver was incrementally moved farther away. A sketch of the corresponding ray paths is shown in (b) with a synthetic velocity–depth function color coded. The labels of example rays and their incidence angles are presented in Eqs. (1)–(10).

tors from being handed downwards, we refine the method by parameterizing a monotonic depth–density function, and by inverting simultaneously for a set of parameters specifying the density and all reflector depths, described below.

2.1 Experimental setup

The radar consists of resistively loaded dipole antennas (10 MHz) linked to a 4 kV pulser (Kentech) for transmitting, and to a digitizing oscilloscope (National Instruments, USB-5133) for receiving (Matsuoka et al., 2012a). Figure 1 illustrates the acquisition geometry in which the transmitter remained at a fixed location and the receiver was moved incrementally farther away at 2 m intervals. The axis between transmitter and receiver at Sites 1, 2, 4, 5, and 6 (locations, Fig. 2), was aligned across-flow (all antennas are parallel to the flow) because we expect the ice thickness to vary little in the across-flow direction and therefore internal reflectors are less likely to dip. For the same reason, Site 3, which is located inside an ice-shelf channel, was aligned parallel to the channel because in this particular area ice thickness varies mostly in the across-flow direction. The transmitter–receiver distance was determined with measuring tape, and recording was triggered by the direct air wave. The latter is not ideal, and can be improved by using fiber-optic cables. Processing of the radar data included horizontal alignment of the first arrivals (a.k.a. t_0 correction), dewow filtering, Ormsby band-pass filtering, and the application of a depth-variable gain. Because triggering was done with the direct air wave, a static

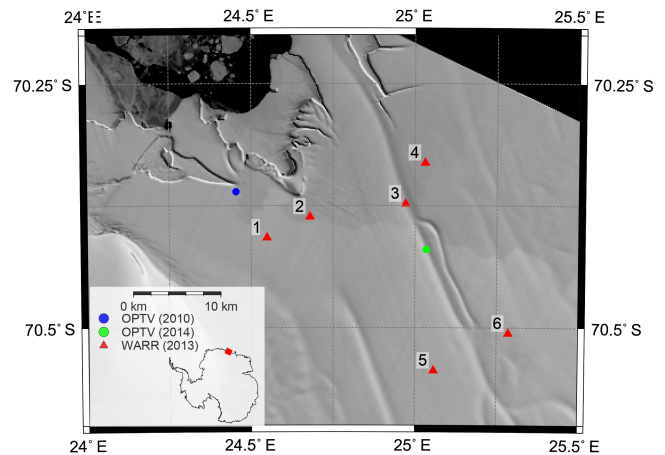


Figure 2. Location of the wide-angle (WARR) radar sites (red triangles) relative to the boreholes of 2010 and 2014 which were used for optical televiewing (OPTV). The depressed surfaces of ice-shelf channels appear as elongated lineations in the background image (Landsat 8, December 2013, provided by the US Geological Survey).

time shift was added to each trace to account for the delayed arrival of the air wave for increasing offsets.

In multi-offset surveys, the traveltime of internal reflectors increases hyperbolically with increasing offset (e.g., Dix, 1955), while the surface wave (traveling in the firm column directly from transmitter to receiver) has a linear moveout.

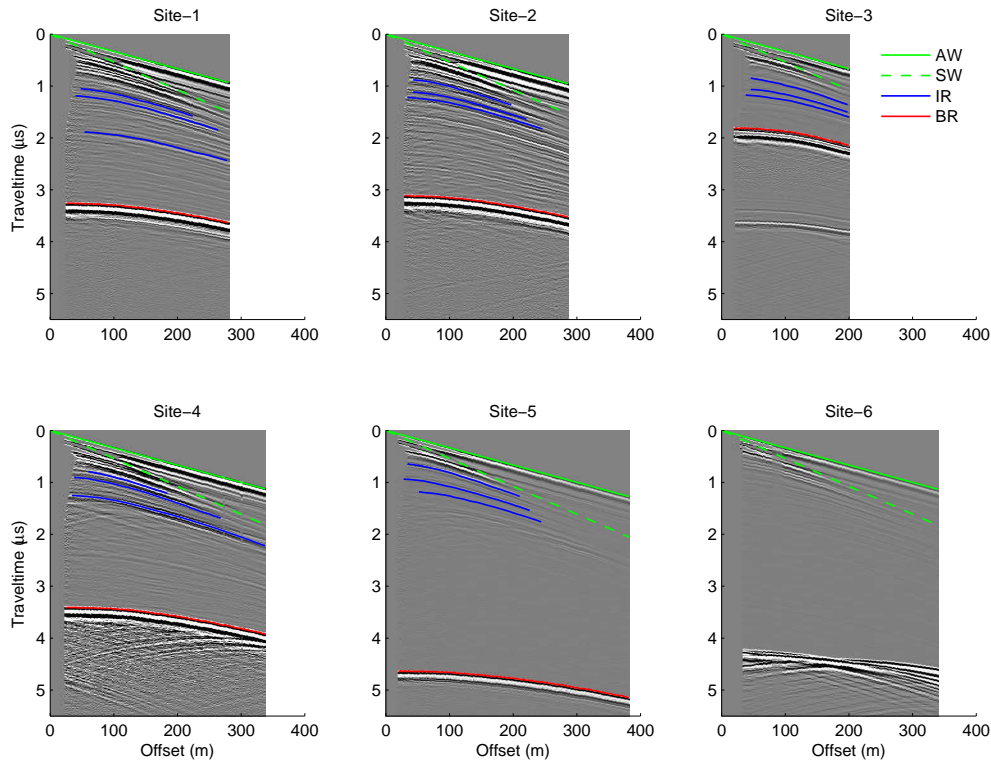


Figure 3. Wide-angle radar data showing air waves (AW, green lines) and surface waves (SW, green dashed lines) with linearly increasing traveltime with offset, while traveltime increases hyperbolically with offset for internal (blue) and basal (red) reflectors. See Fig. 2 for locations of Sites 1–6. Site 6 was excluded from further analysis because the basal reflection is ambiguous (probably due to off-angle reflectors in the vicinity).

The maximum amplitude of the basal reflector was detected automatically and shifted with a constant offset to the first break. Internal reflectors were handpicked. Figure 3 shows radargrams collected at all sites with the picked reflectors that were used for the analysis. The maximum offset for each site was chosen to equal approximately the local ice thickness. At Site 6, basal and internal reflectors are overlaid with signals from off-angle reflectors and cannot be picked unambiguously. We present the data here to exemplify a case for which WARR does not yield reliable results and exclude this site from further analysis.

2.2 Model parameterization and linearization

The traveltime t_{N_r, N_o} of a ray reflected from a reflector N_r ($r \in [1, R]$) at depth D_r measured at offset N_o ($o \in [1, 0]$) is given by a line integral over the inverse of the radio-wave velocity v along the ray path L (extending from the transmitter to the receiver via the reflection boundary).

$$t_{N_r, N_o} = \int_{L(m_v, D_r)} \frac{1}{v(m_v)} dl. \quad (1)$$

Figure 1 illustrates the notation. For each site, we pick a number of reflectors at different depths $m_D = (D_1, \dots, D_R)^T$, and

we parameterize the velocity function as a function of density using the model parameters m_v . We use an inverse method to reconstruct both the reflector depths and the velocity profile from the measured traveltimes.

The traveltime is a non-linear function of the model parameters (and hence the inversion results may be non-unique) because L depends both on the initially unknown radio-wave propagation speed and the reflector depth. The velocity between two radar reflectors is often represented as piecewise constant or piecewise linear (Brown et al., 2012), making the model parameters m_v either the interval velocities or the interval velocity gradients, respectively. Here, we introduce additional constraints from Hubbard et al. (2013) who fit a depth profile of density of the form:

$$\rho = 910 - Ae^{-rz} \quad (2)$$

to density measurements of the borehole recovered at RBIS in 2010. The parameters A and r are tuning parameters for the surface density and the densification length, respectively. We relate density to the radio-wave propagation speed v using the complex refractive index method (CRIM) equation (Wharton et al., 1980; Brown et al., 2012):

$$\rho = \frac{cv^{-1} - 1}{cv_i^{-1} - 1} \rho_i, \quad (3)$$

where $v_i = 168 \text{ m}\mu\text{s}^{-1}$ is the radio-wave propagation speed in pure ice and c is the speed of light in a vacuum.

Combining Eqs. (2) and (3) leads to

$$v(A, r) = \frac{c}{k\rho(A, r) + 1}, \quad (4)$$

with $k = \frac{1}{\rho_i} \left(\frac{c}{v_i} - 1 \right)$ and $\mathbf{m}_v = (A, r)^T$. We use Eq. (4) and assume that (i) radio-wave propagation speed v depends only on density (i.e., excluding ice anisotropy); (ii) density is horizontally homogeneous over the maximum lateral offset of the receiver ($\leq 404 \text{ m}$) but varies with depth so that v only varies with depth in that interval; and (iii) within this interval, internal reflectors are horizontal. We aim to detect lateral variations of the velocity profiles on larger scales (i.e., between Sites 1 and 5) by finding optimal sets of parameters $\mathbf{m} = (\mathbf{m}_D, \mathbf{m}_v) = (A, r, D_1, \dots, D_R)^T \in \mathbb{R}^{N_m}$ describing the data at each site. The number of model parameters $N_m = R + 2$ depends on the number of reflectors.

Using Eq. (4) and approximating the integral through a summation over N_z depth intervals, Eq. (1) reads

$$t_{N_r, N_o}(\mathbf{m}) \approx \frac{1}{c} \sum_{i=1}^{N_z} l_{z_i}(\mathbf{m}) (k\rho(\mathbf{m}_v) + 1). \quad (5)$$

The problem is linearized using an initial guess (marked with superscript 0) and a first-order Taylor expansion:

$$t_{N_r, N_o}(\mathbf{m}) \approx t_{N_r, N_o}^0 + \sum_{j=1}^{N_m} \left. \frac{\partial t_{N_r, N_o}}{\partial m_j} \right|_{m_j^0} (m_j - m_j^0). \quad (6)$$

An equation of type (6) holds for all O offsets of all R reflectors and can be summarized in matrix notation:

$$\boldsymbol{\varepsilon} = \mathbf{S}\boldsymbol{\Delta m}, \quad (7)$$

where we define $\boldsymbol{\varepsilon} = \mathbf{t}_{\text{mod}} - \mathbf{t}_{\text{obs}} \in \mathbb{R}^{N_p}$ as a vector composed of the residuals between the observed (\mathbf{t}_{obs}) and the modeled (\mathbf{t}_{mod}) traveltimes. N_p is the total number of picked datapoints for all reflectors (not all reflectors can be picked to the maximum offset O), $\mathbf{S} \in \mathbb{R}^{N_p \times N_m}$ is a matrix containing all partial derivatives, and $\boldsymbol{\Delta m} \in \mathbb{R}^{N_m}$ is the model update vector. One synthesized reflector is composed of more than 50 independent measurements and at each site $R = 4$ reflectors (including the basal reflector) were picked. There are therefore six model parameters ($N_m = 4 + 2$ for four reflector depths and two parameters A and r describing the depth–density function) and the number of measurements (N_p) is typically larger than 200, turning Eq. (7) into an overdetermined system of equations.

The derivatives of Eq. (6) with respect to A and r are

$$\frac{\partial t_{N_r, N_o}}{\partial A} = -\frac{k}{c} \sum_{i=1}^{N_z} l_{z_i} e^{-rz_i} \quad (8)$$

$$\frac{\partial t_{N_r, N_o}}{\partial r} = \frac{Ak}{c} \sum_{i=1}^{N_z} z_i l_{z_i} e^{-rz_i}, \quad (9)$$

and $\frac{\partial t_{N_r, N_o}}{\partial D_n}$ ($n \in [1, R]$) follows from geometric considerations (Zelt and Smith, 1992):

$$\frac{\partial t_{N_r, N_o}}{\partial D_n} = 2 \frac{\cos \Theta_{N_r, N_o}}{v(D_n)} \delta_{nr}, \quad (10)$$

where Θ_{D_n, N_o} is the incidence angle of ray N_o at the reflector boundary $N_r = n$ (Fig. 1b); $\delta_{nr} = 1$ for $r = n$ and 0 otherwise.

An optimal set of model parameters \mathbf{m} is found as follows. (i) Starting with an initial estimate for the reflector depths \mathbf{m}_{D_0} and the velocity model $\mathbf{m}_{v,0}$, a ray tracing forward model (Sect. 2.3) calculates the expected traveltimes t_{N_r, N_o}^0 for a given set of transmitter–receiver offsets; the difference between modeled and observed traveltimes results in the misfit vector $\boldsymbol{\varepsilon}$ in Eq. (7). (ii) The overdetermined system is inverted for the unknown parameter-correction vector $\boldsymbol{\Delta m}$ (Sect. 2.4), and (iii) the parameter set is updated with $\mathbf{m}^1 = \mathbf{m}^0 + \boldsymbol{\Delta m}$ and serves as new input for the forward model. These steps are repeated iteratively until the parameter updates are negligible.

2.3 Ray tracing forward model

We apply the ray tracing model provided by Margrave (2011) only to reflected (and not to refracted) rays. For a given set of reflectors in a $v(z)$ medium, no analytical solution exists which directly provides a ray path from the transmitter to a given offset via a reflection boundary. The problem is solved iteratively by calculating fans of rays with varying take-off angles until one ray endpoint emerges within a given minimum distance ($\leq 0.5 \text{ m}$) to the receiver. For some $v(z)$ configurations no such ray can be found, indicating that the prescribed $v(z)$ medium does not adequately reproduce the observations.

2.4 Inversion

To solve the inverse problem we seek the set of parameters \mathbf{m} that minimizes the cost function J :

$$J = \frac{1}{2} \boldsymbol{\varepsilon}^T \mathbf{C}_t^{-1} \boldsymbol{\varepsilon} + \frac{1}{2} \lambda (\mathbf{m} - \mathbf{m}^0)^T \mathbf{C}_m^{-1} (\mathbf{m} - \mathbf{m}^0), \quad (11)$$

in which the first term is the ℓ^2 norm of the traveltime residual vector weighted with $\mathbf{C}_t = \text{diag}\{\sigma_i^2\}$, where σ_i is the uncertainty of the traveltime picks. The second term is a regularization (weighted with $\mathbf{C}_m = \text{diag}\{\sigma_j^2\}$, where σ_j is the estimated uncertainty of the model parameters) penalizing solutions which are far from the initial guess. Regularization

with the Lagrange multiplier λ is needed because outliers in the data are weighted disproportionately in a least-squares sense, which can lead to overfitting the data.

We minimize J by updating \mathbf{m} iteratively according to the Gauss–Newton method:

$$\mathbf{m}^{i+1} = \mathbf{m}^i - \left(\mathbf{S}^T \mathbf{C}_t^{-1} \mathbf{S} + \lambda \mathbf{C}_m^{-1} \right)^{-1} \nabla J, \quad (12)$$

with $\nabla J = \mathbf{C}_t^{-1} \mathbf{S} \boldsymbol{\varepsilon} + \lambda \mathbf{C}_m^{-1} (\mathbf{m} - \mathbf{m}^0)$. High values of λ result in a final model vector remaining close to the initial guess; lower values of λ allow for larger changes in the parameter updates. We stop iterating when changes in J are below an arbitrarily small threshold.

2.5 Sensitivity of the firn-air content

In order to compare different measurements at different locations, we decompose the ice shelf into two layers of ice (H_i) and air (H_A) so that $\bar{\rho}H = \rho_i H_i + \rho_a H_A$ and $H_i + H_a = H$ (i.e., $H_A = \frac{\bar{\rho} - \rho_i}{\rho_a - \rho_i} H$). The firn-air content H_A (with air density ρ_a) is a quantity independent of the local ice thickness (as long as the depth-averaged radio-wave speed is determined below the firn–ice transition) and changes thereof indicate changes in the depth-averaged density due to a changing firn-layer thickness. The firn-air content in Antarctica can vary from $H_A = 0$ m in blue ice areas up to $H_A = 45$ m for cold firn on the Antarctic plateau (Ligtenberg et al., 2014). Using the CRIM equation to determine H_A results in

$$H_A = \frac{cH\rho_i \left(\frac{1}{\bar{v}} - \frac{1}{v_i} \right)}{(\rho_a - \rho_i) \left(\frac{c}{v_i} - 1 \right)}. \quad (13)$$

We consider errors in H_A from uncertainties in the depth-averaged radio-wave propagation speed (\bar{v}), and uncertainties in ice thickness (H):

$$\delta H_A^2 \approx \left(\frac{c\rho_i}{v^2(\rho_a - \rho_i) \left(\frac{c}{v_i} - 1 \right)} H \delta \bar{v} \right)^2 + \left(\frac{c\rho_i \left(\frac{1}{\bar{v}} - \frac{1}{v_i} \right)}{(\rho_a - \rho_i) \left(\frac{c}{v_i} - 1 \right)} \delta H \right)^2. \quad (14)$$

Assuming $\delta \bar{v} \approx 1\%$, and $\delta H \approx 10\%$ renders the first term of Eq. (14) about 8 times larger than the second for the parameter ranges considered here, and we therefore neglect errors in ice thickness for the error propagation. Equation (14) shows that the uncertainty of H_A scales with the local ice thickness so that small errors in the depth-averaged velocities ($< 1\%$) result in significant errors in terms of H_A . We use H_A as a sensitive metric, both for comparing sites laterally and illustrating uncertainties of the radar method. In the following, we use synthetic data to choose optimal parameters for the inversion, and to investigate how errors in the data propagate into the final depth–density estimates.

2.6 Testing with synthetic examples

To test the inversion algorithm we use ray tracing with a prescribed depth–density function and recording geometry ($A = 460 \text{ kg m}^{-3}$, $r = 0.033 \text{ m}^{-1}$; transmitter–receiver offsets between 30 and 300 m with 2 m spacing) to create a synthetic traveltimes data set with multiple reflectors. We first investigate whether the solution is well constrained for ideal cases, and then we discuss effects of systematic and random errors in the data.

We consider two ideal cases: a single reflector at 400 m depth, and two reflectors at 30 and 400 m depth. Using the forward model, we simulated a new set of reflectors with model parameters covering depth ranges of ± 5 m from the ideal depths and depth–density functions defined by $r = 0.01 - 0.1 \text{ m}^{-1}$ (A was fixed). This density range corresponds to firn-air contents from $H_A = 5$ to 50 m. The root-mean-square differences (Δt_{rms}) between the perturbed and the ideal reflector are equivalent to the first term of the objective function J (Eq. 11) and indicate how well constrained the solution is. Figure 4a illustrates that for a single reflector the solution is not well constrained, meaning that different sets of model parameters give similar results to the ideal solution (i.e., dense firn/shallower reflector or less dense firn/deeper reflector). For example, positioning the reflector at 392 m depth with $r = 0.063 \text{ m}^{-1}$ results in a firn-air content of ~ 11 m, whereas positioning the reflector at 410 m depth with $r = 0.014 \text{ m}^{-1}$ corresponds to a firn-air content of approximately 40 m. Both cases have a small model–data discrepancy and are barely distinguishable from the ideal solution. Using two reflectors simultaneously better constrains the solution, particularly if the shallower reflector is above the firn–ice transition (Fig. 4b). We conclude from these simple test cases that using the basal reflector alone is inadequate. Instead, multiple reflectors should be considered and inverted for simultaneously. Using this type of testing, we also find (i) that treating A as a free parameter introduces significant tradeoffs with r even for small noise levels. We therefore keep A fixed and assume in the following that the surface density is laterally uniform; (ii) plotting both terms of the objective function J (Eq. 11) versus each other for different λ (a.k.a. L-curve) helps to choose an optimal λ . We find that $\lambda \approx 0.1$ marks approximately the kink point between too large a model–data discrepancy on the one hand and overfitting on the other hand. We keep $\lambda = 0.1$ from hereon to prevent overfitting, but note that results are largely independent of λ for $\lambda \ll 0.1$.

Next, we consider effects of random and systematic errors and simulate four ideal reflectors ($D_1 = 100$ m, $D_2 = 150$ m, $D_3 = 200$ m, $D_4 = 400$ m) to which we add normally distributed noise (i.e., simulating picking errors and variability in aligning the direct waves used for triggering) and linear trends (i.e., simulating accumulated errors in positioning, unaccounted reflector dipping, etc.). We then test the robustness of the inversion for different initial guesses, and differ-

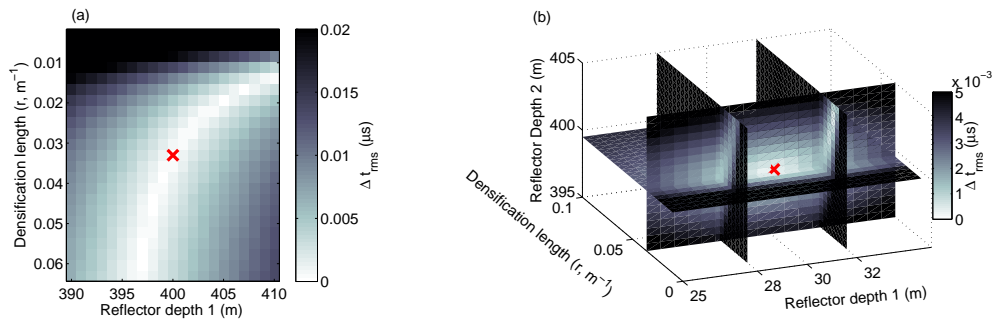


Figure 4. Traveltime residuals (Δt_{rms}) calculated with ray tracing between ideal reflector in a fixed depth–density profile ($A = 460 \text{ kg m}^{-3}$; $r = 0.033 \text{ m}^{-1}$) with reflectors perturbed in terms of depths and density. Ideal solutions are marked with red crosses: **(a)** traveltime residuals for an ideal reflector at 400 m depth; **(b)** volumetric slice plot of traveltime residuals for two idealized reflectors at 30 and 400 m depth.

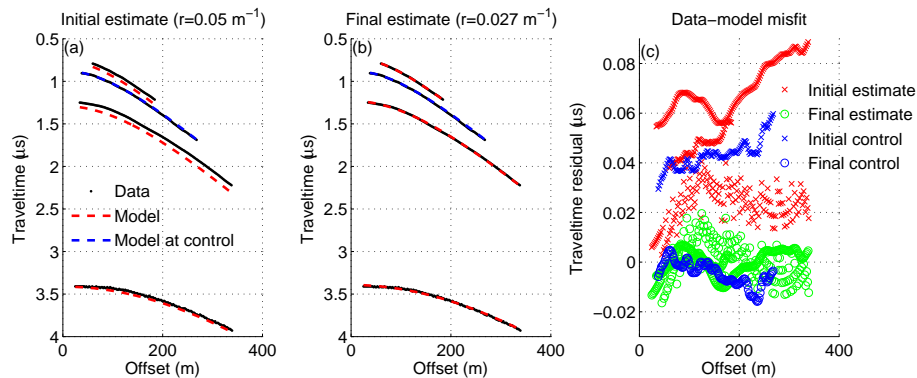


Figure 5. Example for initial **(a)** and final **(b)** fit between the ray tracing forward model and the reflectors at Site 2. In this case, three reflectors (black dots) were used for the inversion and one reflector was kept for control. The forward model corresponds to the red dashed curves and the control reflectors to the blue dashed curves. Initial estimates shown here were $r^0 = 0.05 \text{ m}^{-1}$, $D_1 = 68.2 \text{ m}$, $D_3 = 112.9 \text{ m}$, $D_4 = 291.2 \text{ m}$; the best fit resulted in $r = 0.027 \text{ m}^{-1}$, $D_1 = 67.7 \text{ m}$, $D_3 = 111.2 \text{ m}$, and $D_4 = 293.3 \text{ m}$. The traveltime residual between the model and data for initial **(x)** and final fit **(o)** is shown in **(c)**.

ent magnitudes of noise and systematic errors. We find that the limiting factor for the initial depth guess is the forward model which does not find ray paths for all offsets if the initial guess is further than $\sim 15 \text{ m}$ from the true solution. For all initial guesses deviating less than that, the inversion recovers the true depths robustly within decimeters, even for noise levels with a mean amplitude of 5 times the sampling interval ($0.01 \mu\text{s}$). However, the inversion is most sensitive to trends in the data. For example, if reflectors deviate systematically from 0.04 to $-0.04 \mu\text{s}$ for large offsets, reflector depths are reconstructed with an error of $2\text{--}3 \text{ m}$. The corresponding densities deviate in terms of firn-air content more than 5 m from the ideal solutions. We conclude from these test cases that reflectors need to be picked accurately (i.e. keeping the same phase within the individual wavelets); if systematic differences between the forward model and data occur (e.g., the modeled reflector is tilted with respect to the observations), then results should be interpreted with care.

2.7 Inversion of field data

For each site, three internal reflectors were handpicked ($D_1\text{--}D_3$) to complement the automatically detected basal reflector (D_4 , Fig. 3). Initial guesses for reflector depths are based on standard linear regression in the traveltime²–offset² diagrams (Dix, 1955); $r^0 = 0.033 \text{ m}^{-1}$ and $A = 460 \text{ kg m}^{-3}$ stem from the 2010 OPTV density profile (Hubbard et al., 2013).

We first checked the consistency of the picked internal reflectors and inverted for r and the depths of one internal reflector together with the basal reflector. The remaining two internal reflectors were not used for the inversion, but to validate the results. We did this for all three combinations ($D_1\text{--}D_4$, $D_2\text{--}D_4$, $D_3\text{--}D_4$) in order to check whether internal reflectors had been picked with the correct phase. Results were considered consistent if the model–data discrepancy for each reflector was within $\pm 0.02 \mu\text{s}$ (cf. radar sampling interval is $0.01 \mu\text{s}$). Picking a wrong phase typically causes inconsistent results for one of the combinations. In such a case the corresponding reflector was repicked.

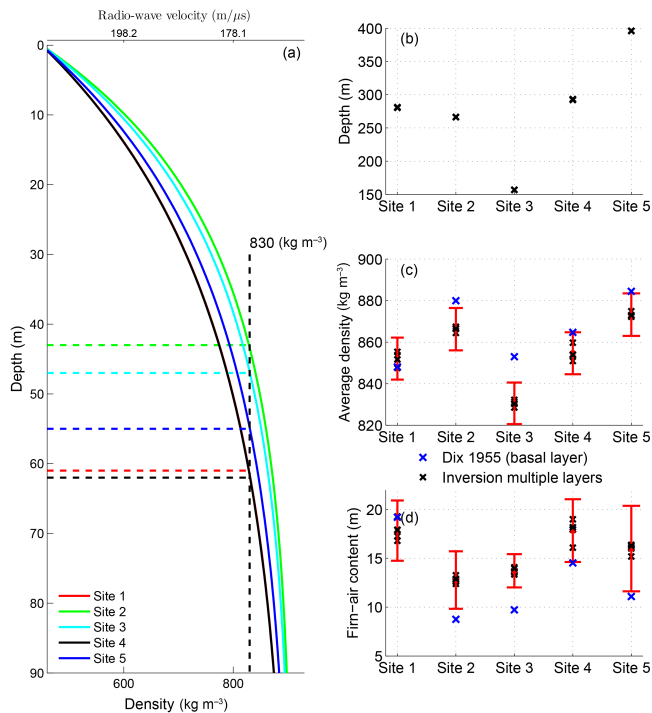


Figure 6. Derived data summary of all sites (Site 3 is located in an ice-shelf channel): **(a)** depth–density profiles inverted from four reflectors, **(b)** ice thickness, **(c)** depth-averaged density, and **(d)** firm-air content. Black crosses in **(b–d)** represent the outcomes for five combinations containing three or more reflectors. Error bars assume a 1 % error in depth-averaged radio-wave propagation speed. The blue crosses correspond to depth-averaged solutions using normal moveout of the basal reflector only (Dix, 1955).

In a second step, we inverted for all five remaining reflector combinations containing three and four reflectors. We also considered a range for r^0 between 0.021 and 0.056 m^{-1} , corresponding to a firm-air content of 24 and 9 m, respectively. Figure 5 illustrates an example where three reflectors were used for the inversion and one was left for validation; the model–data discrepancy is large for the initial guess. After the inversion, the model–data discrepancy is smaller for all reflectors including the reflector that was used for control only.

In general, the final results are more sensitive to the respective reflector combination than to the initial guess of r^0 . For the latter we chose the one resulting in the smallest model–data discrepancy ($r^0 = 0.033 \text{ m}^{-1}$). Differences between the final five parameter sets give a lower boundary for an error estimate.

3 Density from optical televiewing

Densities were evaluated independently from the radar analyses using OPTV logs of two boreholes drilled in 2010 and 2014 (Fig. 2). OPTV exploits the density dependence

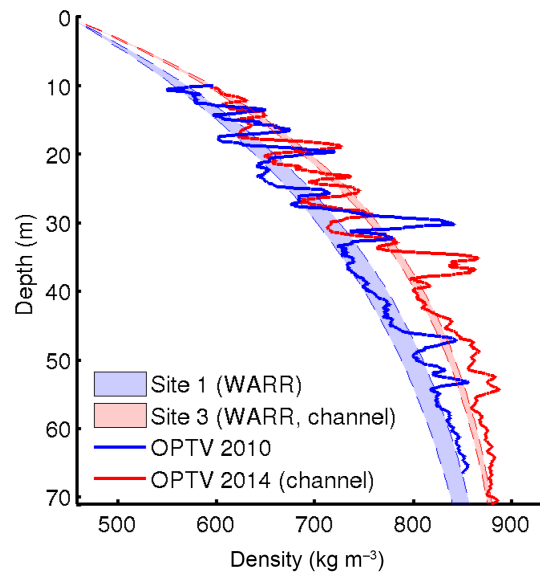


Figure 7. Depth profiles of density derived from WARR (dashed) and OPTV (solid). WARR data are from Sites 1 and 3, closest to the OPTV sites. Site 3 and the 2014 borehole are both in the trough of an ice-shelf channel (Fig. 2). The envelopes of the radar-derived densities correspond to the lower and upper limit of five reflector combinations used for the inversion. The OPTV logs were smoothed with a 0.5 m running mean.

of backscattered light within the borehole. By lowering an OPTV device into boreholes, luminosity (i.e., density) profiles can be collected with a vertical resolution of millimeters (Hubbard et al., 2008). This has been demonstrated for the 2010 borehole at RBIS (Hubbard et al., 2013) and we refer to this reference for further details on the method. Both borehole OPTV logs were calibrated against at least 40 density measurements made directly on core samples, yielding an R^2 value between luminosity and density of 0.96 for the 2010 log (Hubbard et al., 2013) and 0.82 for the 2014 log.

4 Results

Figure 6 and Table 1 summarize the derived depth–density functions, ice thicknesses, radio-wave propagation speeds, depth-averaged densities, and the firm-air contents of the five WARR sites. The reconstructed thicknesses vary between 157 and 396 m (86 % percentage difference), the depth-averaged densities vary between 828 and 874 kg m^{-3} (~ 5 % percentage difference), and corresponding firm-air contents vary from 13.2 to 19.3 m (38 % percentage difference). For the five different reflector combinations at each site, the inverted ice thicknesses differ by less than 1.5 m (< 1 % percentage difference), the inverted depth-averaged densities differ by less than 10 kg m^{-3} (< 1 % percentage difference), and the final firm-air contents differ by less than 3 m (< 17 % percentage difference; Fig. 6b–d). This indicates that the re-

Table 1. Summary of the WARR results from sites 1–5 in terms of range of offsets, number of offsets (O), ice thickness (H), depth-averaged density ($\bar{\rho}$), depth-averaged radio-wave propagation speed (\bar{v}), firn-air content (H_A), the decay length (r) parameterizing the depth–density function, and the deviation from hydrostatic equilibrium (ΔH). The ranges correspond to the lower and upper limits of five reflector combinations at each site (four reflector combinations contain three reflectors, and one combination contains all four reflectors).

No.	Offset (m)	O	H (m)	$\bar{\rho}$ (kg m^{-3})	\bar{v} ($\text{m } \mu\text{s}^{-1}$)	H_A (m)	r (m^{-1})	ΔH (m)
1	26–308	141	280.2–281.3	847–855	173.0–173.8	16.8–19.3	0.026–0.030	15
2	30–318	144	266.1–266.6	864–867	171.9–172.2	12.4–13.2	0.039–0.041	19
3	20–222	101	156.7–157.0	828–832	175.2–175.5	13.3–14.0	0.036–0.038	–4
4	25–366	170	292.9–293.4	850–859	172.6–173.4	16.1–19.0	0.027–0.032	5
5	20–404	142	395.0–396.1	872–874	171.2–171.5	15.2–16.4	0.031–0.036	–13

sults are numerically robust to the combination of reflectors used, and that the local ice thickness and depth-averaged density can be determined with high confidence. However, we cannot derive rigorous error estimates from the inversion itself. We found that picking the internal reflectors is the most sensitive step and, similar to Brown et al. (2012), we estimate that the depth-averaged velocity can be determined within $\pm 1\%$. We used this value to calculate errors for the depth-averaged densities and the equivalent firn-air content. These errors roughly take into account the assumptions of non-dipping reflectors, ice isotropy, and uncertainties of the density–permittivity model.

The estimated 1% error on the (depth-averaged) radio-wave propagation speed translates into large error bars for the corresponding firn-air contents (Fig. 6d), impeding the comparison between sites. Nevertheless, Sites 2 and 3 show lower firn-air contents (~ 13 m) than the other sites (~ 17 m).

To assess the derived depth–density profiles with an independent data set, we compare Site 1 and Site 3 with the OPTV densities from the 2010 and 2014 boreholes, respectively (Fig. 7). Site 3 is located inside an ice-shelf channel, about 10 km north of the 2014 borehole located in the same channel. Site 1 is about 6 km south of the 2010 borehole (Fig. 2). Both radar WARR measurements and the OPTV logs show a depth–density profile that is denser inside than outside the ice-shelf channel. This increases our confidence that the WARR method developed here indeed picks up significant differences in firn-air content on small spatial scales.

5 Discussion

5.1 Benefits of traveltimes inversion using ray tracing

A difference between the new study presented here and previous ones (e.g., Brown et al., 2012) is how the radio-wave propagation speed is parameterized. Previous studies used piecewise linear or uniform speed between individual reflectors, while we parameterize the speed as a continuous function of depth (Eq. 4). Here, we examine the benefit of this approach for interpreting the radar results

A common problem when using the Dix inversion or semblance analysis is that the applied normal moveout (NMO) approximation presupposes small reflection angles (to linearize trigonometric functions) and small velocity contrasts (Dix, 1955). In our case reflection angles can be large ($< 45^\circ$), particularly near the maximum offsets; contrary to NMO, ray tracing is not adversely influenced by wide incidence angles. NMO presupposes small velocity contrasts, because ray paths are approximated as oblique lines neglecting raybending from a gradually changing background medium. Traveltimes inversion with ray tracing equally relies on this approximation as long as interval velocities are assumed. In this study, we prescribe a realistic shape of a depth–density/velocity function, which changes gradually with depth, and raybending is taken into account adequately during the ray tracing. We have tested both the small angle and the small velocity contrast limitations quantitatively by using the OPTV-based depth–density/velocity function and ray tracing in order to simulate synthetic traveltimes of reflectors at various depths (50–500 m) and horizontal offsets (50–500 m). We then used the synthetic traveltimes for calculating the reflector depths and the depth-averaged velocities (averaged from the surface to the reflector depths) subject to the NMO equations. Differences in depth-averaged velocities were smaller than 0.5%, and differences in reflector depths were smaller than 0.5 m. Similar to the findings of Barrett et al. (2007), this confirms that in our case the NMO approximation essentially holds, even for comparatively large horizontal offsets and a continuously changing depth–velocity function. This must not always be the case and ray tracing easily allows the NMO approximation to be checked for each specific setting. For the examples considered here, solutions based on the Dix inversion, using only the basal reflector, typically result in thicker ice and higher depth-averaged densities (and correspondingly lower firn-air contents, Fig. 6c–d).

Data collection in a WARR survey is faster than a common-midpoint survey because only the receiver (or transmitter) needs to be repositioned. A common-midpoint survey, on the other hand, more easily facilitates the corrections for dipping reflectors using dip-moveout (Yilmaz,

1987). The choice for the acquisition geometry thus depends on the time available in the field and on the glaciological setting (i.e., whether dipping reflectors are to be expected). Traveltimes inversion can cope with both types of acquisition geometries. If reflector dips are important, the routine presented here can be adapted to include one dip angle per reflector in the inversion. However, given that including the surface density as an additional free parameter is difficult if all parameters are inverted simultaneously, an iterative approach may be required to find one depth–density function for all reflectors while solving for the reflector dips individually (layer stripping; Brown et al., 2012).

The main advantages of the method applied here are primarily linked to a more robust inversion, which is less sensitive to reflector delineation because reflectors are inverted simultaneously to constrain the density profile. First, prescribing a global depth–density/velocity function for all internal reflectors allows the coherency of the reflector picking to be checked by investigating different subsets of reflector combination to single out reflectors, which were picked with the wrong phase (Sect. 2.7). This step is important, particularly when using lower frequencies as was the case here (10 MHz). At this stage the basal reflector is useful, because it can be identified unambiguously. Once more than two shallow internal reflectors are reliably picked, we found that the inversion results were largely independent of the inclusion of the basal reflector. Second, by inverting for reflectors simultaneously, it is less likely that deeper reflectors inherit uncertainties from shallower reflectors. This can happen when solving for reflectors individually where tradeoffs between interval velocities and reflector depths are subsequently handed downwards. Third, when using interval velocities, the parameter set describing the depth–density/velocity function is larger than is the case here. For example, for four reflectors eight parameters are required when using interval velocities (four velocities and reflector depths, respectively), and this compares with only the five parameters that we required for the method applied here (r and four reflector depths). Simpler models with fewer model parameters are preferable when using inversion.

Based on our synthetic examples, we found that the travel-time inversion used here is unstable if all parameters (surface density, densification length, reflector depths) are inverted for simultaneously. We therefore considered the surface density to be laterally uniform, which is not supported by empirical data. In principle, the surface density can be estimated from the data by picking the linear moveout of the surface wave (green dashed lines in Fig. 3, cf. Brown et al., 2012). However, in our 10 MHz data set the surface wave cannot be identified unambiguously, resulting in a large range of possible surface densities. We addressed this point with a sensitivity analysis including a range of surface densities ($300 \leq A \leq 500 \text{ kg m}^{-3}$). The smallest model–data discrepancies are found with $A \approx 400 \text{ kg m}^{-3}$, but in all cases the final results do not deviate more than the error bars provided

in Fig. 6. This means that the ill-constrained surface density is essentially corrected for during the inversion by adapting the densification length.

The WARR data presented here were collected with a 10 MHz radar. The disadvantage of this low frequency is that fewer reflectors above the firn–ice transition can be picked at this low resolution, relative to higher-frequency data sets (cf. Eisen et al., 2002 who derived an 8 % velocity error with a 25 MHz radar versus a 2 % error with 200 MHz radar). We found that the method applied here can cope with the picking uncertainties at 10 MHz, whereas using Dix inversion frequently resulted in interval densities much larger than the pure ice density. The advantage of using a 10 MHz radar is that the entire ice column is illuminated, including the unambiguous basal reflector. This opens up the possibility for more sophisticated radar-wave velocity models including ice anisotropy originating from aligned crystal orientation fabric below the firn–ice transition (Drews et al., 2012; Matsuoka et al., 2012b). The radar data set is also suited for other glaciological applications, for example, using the basal reflections for deriving ice temperature (via radar attenuation rates) from an amplitude versus offset analysis (Winebrenner et al., 2003) and constraining the alignment of ice crystals using multistatic radar as a large-scale Rigsby stage (Matsuoka et al., 2009).

5.2 Radar- and OPTV-inferred densities

We found velocity models for each site which adequately fit all reflector combinations. There is no systematic deviation larger than the picking uncertainty and hence there is no evidence that reflectors dip within the interval between minimum and maximum offset ($\leq 404 \text{ m}$). The results are numerically robust for different reflector combinations, indicating equal validity for all results based on three reflectors or more (Sect. 2.7).

The derived depth–density functions cluster into two groups: Sites 1, 4, and 5 have a mean firn-air content of $\sim 17 \text{ m}$, whereas Sites 2 and 3 have lower values of $\sim 13 \text{ m}$. While these differences are minor from a radar point of view, they are quite significant from an atmospheric-modeling point of view. For example, van den Broeke et al. (2008) propose that the firn-air content around the entire Antarctic grounding line is bound between 13 m (for the Dronning Maud Land area) and 19 m (for ice shelves in West Antarctica). Including transient effects, such as surface melt, the variability increases but typically stays within 5–20 m (Ligtenberg et al., 2014). Because the aforementioned models run on 27 km grids (approximately the size of our research area) they may overlook effects acting on smaller scales. However, with the estimated uncertainty of the depth-averaged wave speed ($\pm 1 \%$) the radar-derived variability in firn-air content is barely significant (Fig. 6d); notwithstanding, we find that Site 1 (which is closest to the 2010 borehole) agrees closely with the OPTV of 2010, and a similarly

good fit is found between Site 3 and the 2014 OPTV (both located inside the same ice-shelf channel, Fig. 7). The implications are twofold: first, the correspondence between the OPTV-derived density variations and those derived from the WARR method provides independent validation of the latter technique. Second, the fact that both techniques show increased density within the surface channel indicates that the effect is real and should be accounted for by investigations based on hydrostatic equilibrium. However, given that Site 2 also shows a comparatively low firn-air content, we cannot unambiguously conclude from the data alone that firn density is elevated in ice-shelf channels in general. One potential mechanism for such a behavior is the collection of meltwater in the channel's surface depressions. At RBIS, surface melt can be abundant in the (austral) summer months, particularly in an about 20 km wide blue ice belt near the grounding line. The most recent Belgian Antarctic Research Expedition (January 2016) observed frequent melt ponding and refreezing in this area, mostly in the vicinity of ice-shelf channels where meltwater preferentially collects in the small-scale surface depressions. If this holds true, the increased density observed in the WARR data close to the ice-shelf front is an inherited feature from farther upstream. The channel's surface depressions likely also cause a locally increased surface mass balance (Langley et al., 2014), and in general ice-shelf channels can have a particular strain regime (Drews et al., 2015). Both of these factors may also influence the firn densification rate, but given our limited data coverage we refrain from an in-depth analysis here. More work is required to determine whether firn in ice-shelf channels is systematically denser.

Even though uncertainties remain about what causes the density variations, we have shown that traveltime inversion and ray tracing with a prescribed shape for the depth–density function can produce results, which compare closely with densities derived from OPTV (excluding small-scale variability due to melt layers). The data presented here show that a lateral density variability requires attention, particularly when using mass conservation to derive basal melt rates in ice-shelf channels. Errors in the firn-air content propagate approximately with a factor of 10 into the hydrostatic ice thickness, which then substantially alters the magnitude of derived basal melt rates. Using the same parameters as Drews et al. (2015), we compare the WARR-derived ice thickness with the hydrostatic ice thickness for each site. We find a maximum deviation of 19 m for Site 2, and a minimum deviation of 4 m for Site 3 (Table 1). Assuming the absence of marine ice, those deviations are comparatively small given the uncertainties of the geoid and the mean dynamic topography, both of which are required parameters for the hydrostatic inversion.

6 Conclusions

We have collected six wide-angle radar measurements on RBIS and used traveltime inversion in conjunction with ray tracing to infer the local depth–density profiles. In the inversion, we prescribed a physically motivated shape for the depth–density function, which adequately takes curved ray paths and large reflection angles into account and allows the simultaneous inversion of multiple reflectors. We find that this method produces robust results, even with a comparatively low-frequency (10 MHz) radar system with correspondingly reduced spatial resolution and small numbers of internal reflectors used to constrain the density model. The inversion method is flexible and can be adapted to other acquisition geometries and radar frequencies. Ice thickness and depth-averaged densities/wave speed are reconstructed within a few percent. Larger errors in the corresponding firn-air contents, however, impede detailed comparison between sites. Nevertheless, spatial variations in densities derived from both wide-angle radar and borehole optical televiewing show that se-2015-112 the depth–density profile within a 2 km wide ice-shelf channel is denser inside than outside that channel. This density anomaly needs to be accounted for when using hydrostatic equilibrium to infer ice thickness, and has implications for using mass budget methods to determine basal melting in ice-shelf channels. More data are needed to evaluate whether the density anomaly observed here is a generic feature of ice-shelf channels in Antarctica.

Acknowledgements. This paper forms a contribution to the Belgian Research Programme on the Antarctic (Belgian Federal Science Policy Office), project SD/SA/06A “Constraining ice mass changes in Antarctica” (IceCon), as well as the FNRS-FRFC (Fonds de la Recherche Scientifique) project IDyRA. We thank the InBev Baillet Latour Antarctica Fellowship for financing the RBIS fieldwork and the International Polar Foundation for providing all required logistics in the field. We thank in particular A. Hubert, K. Moerman, K. Soete, and L. Favier for support in the field. Morgane Philippe is partially funded through a grant from the “Fonds David et Alice Van Buuren”. The comments of two reviewers and the editor R. Bingham have improved the initial version of this manuscript. A version of the code is accessible on request and on GitHub (<https://github.com/rdrews/>).

Edited by: R. Bingham

References

- Arthern, R. J., Vaughan, D. G., Rankin, A. M., Mulvaney, R., and Thomas, E. R.: In situ measurements of Antarctic snow compaction compared with predictions of models, *J. Geophys. Res.*, 115, F03011, doi:10.1029/2009jf001306, 2010.
- Arthern, R. J., Corr, H. F. J., Gillet-Chaulet, F., Hawley, R. L., and Morris, E. M.: Inversion for the density-depth profile of polar firn

- using a stepped-frequency radar, *J. Geophys. Res.-Earth*, 118, 1257–1263, doi:10.1002/jgrf.20089, 2013.
- Barrett, E. B., Murray, T., and Clark, R.: Errors in Radar CMP Velocity Estimates Due to Survey Geometry, and Their Implication for Ice Water Content Estimation, *J. Environ. Eng. Geoph.*, 12, 101–111, doi:10.2113/JEEG12.1.101, 2007.
- Bender, M., Sowers, T., and Brook, E.: Gases in ice cores, *P. Natl. Acad. Sci. USA*, 94, 8343–8349, doi:10.1073/pnas.94.16.8343, 1997.
- Blindow, N., Suckro, S. K., Rückamp, M., Braun, M., Schindler, M., Breuer, B., Saurer, H., Simões, J. C., and Lange, M. A.: Geometry and thermal regime of the King George Island ice cap, Antarctica, from GPR and GPS, *Ann. Glaciol.*, 51, 103–109, doi:10.3189/172756410791392691, 2010.
- Booth, A., Clark, R., and Murray, T.: Semblance response to a ground-penetrating radar wavelet and resulting errors in velocity analysis, *Near Surf. Geophys.*, 8, 235–246, doi:10.3997/1873-0604.2011019, 2010.
- Booth, A., Clark, R., and Murray, T.: Influences on the resolution of GPR velocity analyses and a Monte Carlo simulation for establishing velocity precision, *Near Surf. Geophys.*, 9, 399–411, doi:10.3997/1873-0604.2011019, 2011.
- Bradford, J. H., Harper, J. T., and Brown, J.: Complex dielectric permittivity measurements from ground-penetrating radar data to estimate snow liquid water content in the pendular regime, *Water Resour. Res.*, 45, W08403, doi:10.1029/2008WR007341, 2009.
- Brown, J., Bradford, J., Harper, J., Pfeffer, W. T., Humphrey, N., and Mosley-Thompson, E.: Georadar-derived estimates of firn density in the percolation zone, western Greenland ice sheet, *J. Geophys. Res.*, 117, F01011, doi:10.1029/2011JF002089, F01011, 2012.
- Cuffey, K. and Paterson, W.: *The physics of Glaciers*, 4th Edn., Burlington, MA, Academic Press, 2010.
- Depoorter, M. A., Bamber, J. L., Griggs, J. A., Lenaerts, J. T. M., Ligtenberg, S. R. M., van den Broeke, M. R., and Moholdt, G.: Calving fluxes and basal melt rates of Antarctic ice shelves, *Nature*, 502, 89–92, doi:10.1038/nature12567, 2013.
- Dix, C. H.: Seismic Velocities from Surface Measurements, *Geophysics*, 20, 68–86, doi:10.1190/1.1438126, 1955.
- Drews, R.: Evolution of ice-shelf channels in Antarctic ice shelves, *The Cryosphere*, 9, 1169–1181, doi:10.5194/tc-9-1169-2015, 2015.
- Drews, R., Eisen, O., Steinhage, D., Weikusat, I., Kipfstuhl, S., and Wilhelms, F.: Potential mechanisms for anisotropy in ice-penetrating radar data, *J. Glaciol.*, 58, 613–624, doi:10.3189/2012JoG11J114, 2012.
- Drews, R., Matsuoka, K., Martín, C., Callens, D., Bergeot, N., and Pattyn, F.: Evolution of Derwael Ice Rise in Dronning Maud Land, Antarctica, over the last millennia, *J. Geophys. Res.-Earth*, 120, 564–579, doi:10.1002/2014JF003246, 2015.
- Dutrieux, P., Vaughan, D. G., Corr, H. F. J., Jenkins, A., Holland, P. R., Joughin, I., and Fleming, A. H.: Pine Island glacier ice shelf melt distributed at kilometre scales, *The Cryosphere*, 7, 1543–1555, doi:10.5194/tc-7-1543-2013, 2013.
- Eisen, O., Nixdorf, U., Wilhelms, F., and Miller, H.: Electromagnetic wave speed in polar ice: validation of the common-midpoint technique with high-resolution dielectric-profiling and -density measurements, *Ann. Glaciol.*, 34, 150–156, doi:10.3189/172756402781817509, 2002.
- Eisen, O., Frezzotti, M., Genthon, C., Isaksson, E., Magand, O., van den Broeke, M. R., Dixon, D. A., Ekaykin, A., Holmlund, P., Kameda, T., Karlöf, L., Kaspari, S., Lipenkov, V. Y., Oerter, H., Takahashi, S., and Vaughan, D. G.: Ground-based measurements of spatial and temporal variability of snow accumulation in East Antarctica, *Rev. Geophys.*, 46, RG2001, doi:10.1029/2006RG000218, 2008.
- Freitag, J., Kipfstuhl, S., and Laepple, T.: Core-scale radioscopic imaging: a new method reveals density–calcium link in Antarctic firn, *J. Glaciol.*, 59, 1009–1014, doi:10.3189/2013JoG13J028, 2013a.
- Freitag, J., Kipfstuhl, S., Laepple, T., and Wilhelms, F.: Impurity-controlled densification: a new model for stratified polar firn, *J. Glaciol.*, 59, 1163–1169, doi:10.3189/2013JoG13J042, 2013b.
- Gladish, C. V., Holland, D. M., Holland, P. R., and Price, S. F.: Ice-shelf basal channels in a coupled ice/ocean model, *J. Glaciol.*, 58, 1227–1244, doi:10.3189/2012JoG12J003, 2012.
- Gregory, S. A., Albert, M. R., and Baker, I.: Impact of physical properties and accumulation rate on pore close-off in layered firn, *The Cryosphere*, 8, 91–105, doi:10.5194/tc-8-91-2014, 2014.
- Griggs, J. and Bamber, J.: Antarctic ice-shelf thickness from satellite radar altimetry, *J. Glaciol.*, 57, 485–498, doi:10.3189/002214311796905659, 2011.
- Hempel, L., Thyssen, F., Gundestrup, N., Clausen, H. B., and Miller, H.: A comparison of radio-echo sounding data and electrical conductivity of the GRIP ice core, *J. Glaciol.*, 46, 369–374, doi:10.3189/172756500781833070, 2000.
- Herron, M. M. and Langway, C. C.: Firn Densification: An empirical Model, *J. Glaciol.*, 25, 373–385, 1980.
- Hörhold, M. W., Kipfstuhl, S., Wilhelms, F., Freitag, J., and Frenzel, A.: The densification of layered polar firn, *J. Geophys. Res.*, 116, F01001, doi:10.1029/2009JF001630, 2011.
- Hörhold, M. W., Laepple, T., Freitag, J., Bigler, M., Fischer, H., and Kipfstuhl, S.: On the impact of impurities on the densification of polar firn, *Earth Planet. Sc. Lett.*, 325–32, 93–99, doi:10.1016/j.epsl.2011.12.022, 2012.
- Hubbard, B. and Glasser, N.: *Field Techniques in Glaciology and Glacial Geomorphology*, John Wiley & Sons Ltd., The Atrium, Southern Gate, Chichester, West Sussex, 2005.
- Hubbard, B., Roberson, S., Samyn, D., and Merton-Lyn, D.: Digital optical televising of ice boreholes, *J. Glaciol.*, 54, 823–830, doi:10.3189/002214308787779988, 2008.
- Hubbard, B., Tison, J.-L., Philippe, M., Heene, B., Pattyn, F., Malone, T., and Freitag, J.: Ice shelf density reconstructed from optical televiewer borehole logging, *Geophys. Res. Lett.*, 40, 5882–5887, doi:10.1002/2013GL058023, 2013.
- Kawamura, T.: Nondestructive, three-dimensional density measurements of ice core samples by X ray computed tomography, *J. Geophys. Res.*, 95, 12407–12412, doi:10.1029/JB095iB08p12407, 1990.
- Kovacs, A., Gow, A. J., and Morey, R. M.: The in-situ dielectric constant of polar firn revisited, *Cold Reg. Sci. Technol.*, 23, 245–256, doi:10.1016/0165-232X(94)00016-Q, 1995.
- Langley, K., von Deschanden, A., Kohler, J., Sinisalo, A., Matsuoka, K., Hattermann, T., Humbert, A., Nøst, O. A., and Isaksson, E.: Complex network of channels beneath an Antarctic ice shelf, *Geophys. Res. Lett.*, 41, 1209–1215, doi:10.1002/2013GL058947, 2014.

- Le Brocq, A., Ross, N., Griggs, J., Bingham, R., Corr, H., Ferraccioli, F., Jenkins, A., Jordan, T., Payne, A., Rippin, D., and Siegert, M.: Evidence from ice shelves for channelized meltwater flow beneath the Antarctic Ice Sheet, *Nat. Geosci.*, 6, 945–948, doi:10.1038/ngeo1977, 2013.
- Lenaerts, J. T. M., Brown, J., van den Broeke, M. R., Matsuoka, K., Drews, R., Callens, D., Philippe, M., Gorodetskaya, I. V., van Meijgaard, E., Reijmer, C. H., Pattyn, F., and van Lipzig, N. P. M.: High variability of climate and surface mass balance induced by Antarctic ice rises, *J. Glaciol.*, 60, 1101–1110, doi:10.3189/2014JG14J040, 2014.
- Ligtenberg, S. R. M., Kuipers Munneke, P., and van den Broeke, M. R.: Present and future variations in Antarctic firn air content, *The Cryosphere*, 8, 1711–1723, doi:10.5194/tc-8-1711-2014, 2014.
- Looyenga, H.: Dielectric constants of heterogeneous mixtures, *Physica*, 31, 401–406, 1965.
- Margrave, G. F.: Numerical Methods of Exploration Seismology with algorithms in Matlab, CREWES Toolbox Version: 1006, CREWES Department of Geoscience, University of Calgary, downloaded January 2015, 2011.
- Matsuoka, K., Wilen, L., Hurley, S. P., and Raymond, C. F.: Effects of Birefringence Within Ice Sheets on Obliquely Propagating Radio Waves, *IEEE T. Geosci. Remote*, 47, 1429–1443, doi:10.1109/TGRS.2008.2005201, 2009.
- Matsuoka, K., Pattyn, F., Callens, D., and Conway, H.: Radar characterization of the basal interface across the grounding zone of an ice-rise promontory in East Antarctica, *Ann. Glaciol.*, 53, 29–34, doi:10.3189/2012AoG60A106, 2012a.
- Matsuoka, K., Power, D., Fujita, S., and Raymond, C. F.: Rapid development of anisotropic ice-crystal-alignment fabrics inferred from englacial radar polarimetry, central West Antarctica, *J. Geophys. Res.*, 117, F03029, doi:10.1029/2012JF002440, 2012b.
- Millgate, T., Holland, P. R., Jenkins, A., and Johnson, H. L.: The effect of basal channels on oceanic ice-shelf melting, *J. Geophys. Res.-Oceans*, 118, 6951–6964, doi:10.1002/2013JC009402, 2013.
- Murray, T., Stuart, G. W., Miller, P. J., Woodward, J., Smith, A. M., Porter, P. R., and Jiskoot, H.: Glacier surge propagation by thermal evolution at the bed, *J. Geophys. Res.*, 105, 13491–13507, doi:10.1029/2000JB900066, 2000.
- Rignot, E., Jacobs, S., Mouginot, J., and Scheuchl, B.: Ice-Shelf Melting Around Antarctica, *Science*, 341, 266–270, doi:10.1126/science.1235798, 2013.
- Sergienko, O. V.: Basal channels on ice shelves, *J. Geophys. Res.-Earth*, 118, 1342–1355, doi:10.1002/jgrf.20105, 2013.
- Stanton, T. P., Shaw, W. J., Truffer, M., Corr, H. F. J., Peters, L. E., Riverman, K. L., Bindschadler, R., Holland, D. M., and Anandakrishnan, S.: Channelized Ice Melting in the Ocean Boundary Layer Beneath Pine Island Glacier, Antarctica, *Science*, 341, 1236–1239, doi:10.1126/science.1239373, 2013.
- van den Broeke, M., van den Berg, W. J., and van den Meijgaard, E.: Firn depth correction along the Antarctic grounding line, *Antarct. Sci.*, 20, 513–517, doi:10.1017/S095410200800148X, 2008.
- Vaughan, D. G., Corr, H. F. J., Bindschadler, R. A., Dutrieux, P., Gudmundsson, G. H., Jenkins, A., Newman, T., Vornberger, P., and Wingham, D. J.: Subglacial melt channels and fracture in the floating part of Pine Island Glacier, Antarctica, *J. Geophys. Res.*, 117, F03012, doi:10.1029/2012JF002360, 2012.
- Waddington, E. D., Neumann, T. A., Koutnik, M. R., Marshall, H.-P., and Morse, D. L.: Inference of accumulation-rate patterns from deep layers in glaciers and ice sheets, *J. Glaciol.*, 53, 694–712, doi:10.3189/002214307784409351, 2007.
- Wharton, R. B., Rau, R., and Best, D. L.: Electromagnetic propagation logging: Advances in technique and interpretation, paper presented at the SPE Annual Technical Conference and Exhibition, Dallas, Texas, 21–24 September, doi:10.2118/9267-MS, 1980.
- Wilhelms, F., Kipfstuhl, S., Miller, H., Heinloth, K., and Firestone, J.: Precise dielectric profiling of ice cores: A new device with improved guarding and its theory, *J. Glaciol.*, 44, 171–174, 1998.
- Winebrenner, D. P., Smith, B. E., Catania, G. A., Conway, H. B., and Raymond, C. F.: Radio-frequency attenuation beneath Siple Dome, West Antarctica, from wide-angle and profiling radar observations, *Ann. Glaciol.*, 37, 226–232, doi:10.3189/172756403781815483, 2003.
- Wouters, B., Martín-Español, A., Helm, V., Flament, T., van Wessem, J. M., Ligtenberg, S. R. M., van den Broeke, M. R., and Bamber, J. L.: Dynamic thinning of glaciers on the Southern Antarctic Peninsula, *Science*, 348, 899–903, doi:10.1126/science.aaa5727, 2015.
- Yilmaz, O.: Seismic Data Processing, Society of Exploration Geophysicists, Tulsa, OK, 1987.
- Zelt, C. A. and Smith, R. B.: Seismic traveltimes inversion for 2-D crustal velocity structure, *Geophys. J. Int.*, 108, 16–34, doi:10.1111/j.1365-246X.1992.tb00836.x, 1992.
- Zwally, H. J. and Jun, L.: Seasonal and interannual variations of firn densification and ice-sheet surface elevation at the Greenland summit, *J. Glaciol.*, 48, 199–207, doi:10.3189/172756502781831403, 2002.